Electrochimica Acta 318 (2019) 635–643

Contents lists available at ScienceDirect

Electrochimica Acta

journal homepage: www.elsevier.com/locate/electacta

V_2O_3/C nanocomposites with interface defects for enhanced intercalation pseudocapacitance

Jiqi Zheng [a, b], Yifu Zhang [a, **], Changgong Meng [a], Xiaofei Wang [a], Chaofeng Liu [b], Mengke Bo [a], Xiaoyu Pei [a], Yuanan Wei [a], Tianming Lv [a], Guozhong Cao [b, *]

[a] School of Chemical Engineering, Dalian University of Technology, Dalian, 116024, PR China
[b] Department of Materials Science and Engineering, University of Washington, Seattle, WA, 98195, USA

ARTICLE INFO

Article history:
Received 7 February 2019
Received in revised form
16 June 2019
Accepted 20 June 2019
Available online 20 June 2019

Keywords:
V_2O_3-Based composites
Highly dispersed nanostructure
Interface defects
Specific intercalation pseudocapacitance

ABSTRACT

V_2O_3 nanoparticles highly dispersed in amorphous carbon composites (VO-C) were successfully synthesized by the calcination of $(NH_4)_2V_3O_8$/C precursor, which was fabricated through the hydrothermal reaction using commercial NH_4VO_3 and glucose as raw materials. The release of gaseous byproduct during the formation of V_2O_3 and amorphous carbon resulted in the formation of highly dispersed oxide nanoparticles dispersed in porous carbon matrix. The composites exhibited a high specific intercalation pseudocapacitance of 458.6 F g^{-1} at 0.5 A g^{-1} with a retention of 86% after 1000 cycles in aqueous electrolyte. Such good electrochemical properties is attributed to the high diffusion coefficient and promoted electron transfer of the composites possibly as a result of surface modification of V_2O_3 nanoparticles. In addition, highly porous carbon network with homogeneously dispersed V_2O_3 permits efficient intercalation reaction with much enhanced stability of V_2O_3. Flexible asymmetric supercapacitors using synthesized VO-C and active carbon electrodes were assembled and demonstrated excellent electrical energy storage performance.

1. Introduction

The development of rechargeable energy storage devices with high performance is considered as one of the effective ways to alleviate the energy crisis by improving the efficiency of energy storage and utilization. Supercapacitors (SCs) have received much attention because they can bridge the gap of power and energy density between batteries and conventional capacitors, as well as their excellent reversibility and long cycling life [1–6]. SCs can be classified into two categories according to their different mechanisms, electrochemical double layer capacitors (EDLCs) and pseudocapacitors. The former stores charges by the adsorption of ions on the electrode-electrolyte interface; while the latter storages charges by faradaic redox reactions of transition metal oxides (TMOs) or conductive polymers, and can display much higher capacitances than EDLCs [7–9]. Though the charge mechanisms of TMO for supercapacitors and batteries are both redox reaction, the mainly difference is that unlike in batteries, the typical pseudocapacitive behavior only occurs near the surface of electrode materials, making the process non-diffusion controlled [10,11]. Whereas, this merit also leads to the low utilization of TMOs compared to batteries. Recently, a new concept "intercalation pseudocapacitance" was proposed, which is generated by intercalation of ions into the bulk materials, and is not limited by the ions diffusion because of the sufficient and accessible ionic pathways of the active material [11–15]. Various kinds of materials with such character were developed, such as TiO_2 [16], HTi_6O_{13} [17], MoO_2 [13], VO_2 [18], etc. Intercalation pseudocapacitive materials combine the advantages of both batteries (high capacitance) and supercapacitors (high rate), making them promising electrode materials for high performance supercapacitors.

As a kind of typical TMOs, vanadium oxides are ideal materials for energy storage because of their abundant sources, variable oxidation states and unique layered structure, which is beneficial for redox reactions and fast diffusion of ions in the 2D interlayers [19–21]. Among numerous vanadium oxides, V_2O_3 exhibits a quasi-metallic behavior with a conductivity of $10^3\ \Omega^{-1}\ cm^{-1}$, which is much higher than V_2O_5 ($10^{-3}\ \Omega^{-1}\ cm^{-1}$) and monoclinic VO_2 ($\approx 4\ \Omega^{-1}\ cm^{-1}$), and comparable with RuO_2 ($10^4\ \Omega^{-1}\ cm^{-1}$), making

* Corresponding author.
** Corresponding author.
E-mail addresses: yfzhang@dlut.edu.cn (Y. Zhang), gzcao@uw.edu (G. Cao).

https://doi.org/10.1016/j.electacta.2019.06.125
0013-4686/

it a suitable material for energy storage [22,23]. According to current research, V_2O_3 has shown huge potential as an anode material for lithium batteries with high capacities [24–26]. However, the reported specific capacitances of V_2O_3-based materials for supercapacitors are less satisfactory, suggesting that existing structures or compositions can't make full use of V_2O_3 [20]. The design and synthesis of new structured V_2O_3-based materials with high performance require further studies. Though synthesis of nanostructured materials is an effective way to improve the utilization of vanadium oxides, it also causes the problem of poor cycling stability because large contact area is created between active material and active oxides, and vanadium oxides are liable to form soluble species in aqueous solutions [27,28]. Previous research has proven that combined nanostructured vanadium oxides with carbon can not only protect them from dissolution and structural deterioration, but also enhance the electron transfer efficiency and prevent the agglomeration of nanoparticles [29]. Several V_2O_5/amorphous carbon composites for high performance supercapacitors were developed [30], such as the amorphous carbon coated V_2O_5 nanorods reported by Saravanakumar et al. [31], which achieved a high specific capacitance of 417 F g^{-1} at 0.5 A g^{-1}. Recently, Zhao et al. [32] synthesized the nest-like V_3O_7 nanowires coated by N-doped carbon exhibited a high specific capacitance of 660 F g^{-1} at 0.5 A g^{-1}. It was also reported B phase and A phase VO_2 and amorphous carbon composites; their specific capacitances are 182 and 144 F g^{-1} at 1 A g^{-1}, respectively [33,34]. V_2O_3-based composites were also studied in recent years. Li et al. [35] reported the in-situ synthesis of V_2O_3 nanoflakes@C core–shell composites using hexadecyltrimethylammonium bromide (CTAB) as the carbon source. The composites exhibited a capacitance of 205 F g^{-1} at 0.05 A g^{-1} in 1 M $NaNO_3$ aqueous solution, which is higher than bulk V_2O_3 (159 F g^{-1}) and 76% of the capacitance can be retained after 500 circles. Hu et al. [36] synthesized hierarchical porous structured V_2O_3@C core-shell nanorods with high surface area, which had a capacitance of 228 F g^{-1} at 0.5 A g^{-1} and retained 81% after 1000 cycles in 5 M LiCl aqueous solution. These works certified that encapsulating V_2O_3 into carbon is a feasible strategy to improve its electrochemical properties, but the poor contact at the interface can still be the drawback of the composites. In this contribution, a highly dispersed architecture with surface-modified V_2O_3 nanoparticles and amorphous carbon was designed and synthesized.

In the present study, V_2O_3 nanoparticles were dispersed in amorphous carbon (VO-C) through the hydrothermal reaction and the subsequent calcination using commercial NH_4VO_3 and glucose as raw materials. Such structure of the composites has several advantages when used as the electrode material for supercapacitors. The modification at the interface is beneficial for the electron transfer; the highly dispersed nano-sized V_2O_3 with crystalline layered structure can enhance the diffusion coefficient of ions; the protection of the outer carbon can improve the cycling stability of the composites. The study of their energy storage mechanism showed that though the capacitance was generated by the intercalation of lithium ions in to V_2O_3 bulk, the process was predominantly non-diffusion controlled in kinetics. Thus, the composites exhibited specific intercalation pseudocapacitance of 458.6 F g^{-1} at 0.5 A g^{-1}, which is higher than the reported V_2O_3-based materials. The excellent electrochemical performance makes the composites a promising electrode material for supercapacitors. The electrochemical properties of the asymmetric supercapacitor device assembled by the as obtained VO-C and active carbon are also studied and used in practical applications.

2. Experimental section

2.1. Synthesis of VO-C

Analytical grade ammonium metavanadate (NH_4VO_3) and glucose ($C_6H_{12}O_6 \cdot H_2O$) were used without further purification in this work. The V_2O_3 nanoparticles highly dispersed on amorphous carbon composites (VO-C) were synthesized through a hydrothermal reaction and the subsequent calcination, as shown in Fig. 1. In detail, 1.98 g of glucose (0.01 mol) was dissolved in 35 mL of distilled water, then 2.43 g of NH_4VO_3 (0.02 mol) was dispersed into the solution through magnetic stirring for 30 min. The mixture was transferred into a 50 mL Teflon-lined stainless-steel autoclave and heated at 180 °C for 12 h. The obtained product was centrifuged, washed with distilled water and ethanol for several times, and dried in vacuum at 75 °C. The obtained $(NH_4)_2V_3O_8$/C precursor was then calcined in a tube furnace at 700 °C (with a heating rate of 5 °C/min) for 2 h to get VO-C. For comparison, amorphous carbon was also synthesized in the same hydrothermal and calcination process using the same amount of glucose as the raw material, and mixed with commercial V_2O_3. The mixture was named as VO+C.

2.2. Material characterizations

X-ray diffraction (XRD) carried out on Panalytical X'Pert powder diffractometer (40 kV, 40 mA) was used to characterize the compositions and structures of the products. Fourier transform infrared

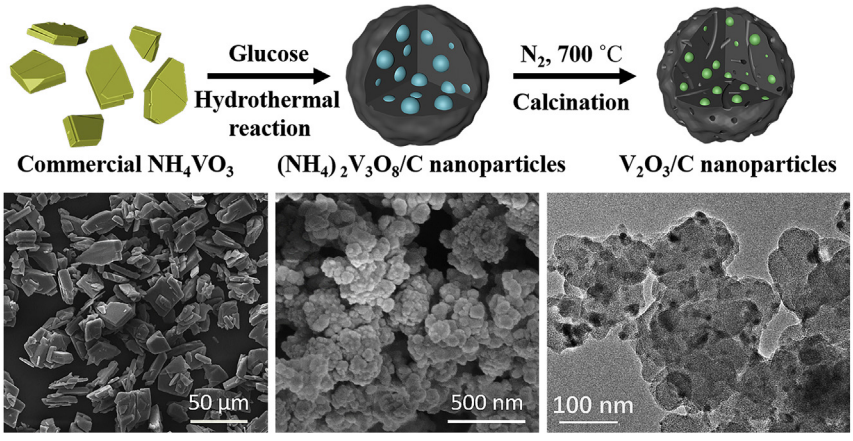

Fig. 1. A schematic illustration of the synthesis of highly dispersed VO-C.

spectroscopy (FTIR) spectra were collected on a Nicolet 6700 spectrometer from 4000 to 400 cm^{-1} using the KBr pellet technique. Raman spectra were recorded on a Thermo Scientific spectrometer with a laser of 532 nm. X-ray photoelectron spectrum (XPS) was taken on a Kratos Axis Ultra DLD spectrometer with monochromatized Al Kα X-ray. Elemental analysis (EA) measurement was carried out on a Vario EL equipment. Differential scanning calorimetry (DSC 3+ STAR^e System, Mettler Toledo) was measured in flowing air (50 sccm) from 40 to 700 °C. The morphologies of the products were characterized by a field-emission scanning electron microscope (FE-SEM, NOVA NanoSEM 450) on which an Energy-dispersive X-ray spectrometer (EDS) is attached to characterize the chemical compositions of the products. Transmission electron microscopy (TEM, FEI TECNAI F30) was used to investigate the nanostructures of the samples. Nitrogen adsorption desorption isotherms were determined by Brunauer-Emmet-Teller (BET) method using Quantachrome Nova 4200e and samples were degassed at 250 °C for 12 h.

2.3. Electrochemical characterizations

Active material, carbon black and polyvinylidene difluoride (PVDF) were mixed in a mass ratio of 8: 1: 1 using N-methyl-2-pyrrolidone (NMP) as the solvent to prepare working electrodes. The obtained slurry was painted on nickel foam and heated at 100 °C to remove NMP, then pressed at 10 MPa. The mass loadings of the working electrodes are about 3 mg cm^{-2}. In the three-electrode experimental system, 5 M LiCl aqueous solution was used as the electrolyte. A Pt wire and a saturated calomel electrode (SCE) were served as the counter electrode and the reference electrode, respectively. Cyclic voltammetry (CV), galvanostatic charge-discharge (GCD) were performed in a potential window of −1.0 to −0.3 V on a CHI 660D electrochemical workstation. Electrochemical impedance spectroscopy (EIS) measurements were tested in the frequency range from 100 kHz to 0.01 Hz. The ion diffusion coefficient of the electrode material was calculated from the low frequency region of EIS plots based on the following equation [37]:

$$D_{Li^+}^{EIS} = \frac{R^2T^2}{2A^2n^4F^4C^2\sigma_w^2} \quad (1)$$

where F (96500 C mol^{-1}) and R (8.314 J mol^{-1} K^{-1}) are the Faraday and gas constant respectively; T (298 K) is the absolute temperature, A (cm^2), C ($mol \cdot cm^{-3}$) and n are the surface area of the electrode, concentration of ion in the electrolyte and number of electrons transferred per molecule, respectively. Warburg coefficient (σ_w) is the slope of Z'-$\omega^{-1/2}$, ω ($Rad \cdot s^{-1}$) is the angular frequency.

The specific capacitance (C, $F \cdot g^{-1}$) can be calculated on the basis of discharge curves according to the equation (2):

$$C = \frac{I \cdot \Delta t}{m \cdot \Delta U} \quad (2)$$

where m (g) is the mass loading of the product on the working electrode; Δt (s) is the discharge time in the potential window ΔU (V) under the charge-discharge current I (A). Flexible asymmetric supercapacitors (ASCs) were fabricated using commercial activated carbon (AC) as the counter electrode and 5 M LiCl/polyvinyl alcohol (PVA) as the electrolyte. A separator (NKK-PF30AC) was sandwiched in between to separate two electrodes. The mass ratio of the two electrodes were optimized based on the following equation to balance the charge:

$$\frac{m_+}{m_-} = \frac{(C_- \cdot \Delta U_-)}{(C_+ \cdot \Delta U_+)} \quad (3)$$

The areal capacitance (C, $F \cdot cm^{-2}$ on S, cm^2), energy density E ($W \cdot h \cdot m^{-2}$) and power density P ($W \cdot m^{-2}$) of ASCs were calculated based on following equations [38]:

$$C_p = \frac{I \cdot \Delta t}{S \cdot \Delta U} \quad (4)$$

$$E = \frac{I}{0.36S} \int_0^t U dt \quad (5)$$

$$P = \frac{3600E}{\Delta t} \quad (6)$$

3. Results and discussion

3.1. Composition and morphology of VO-C

The VO-C was synthesized through a two-step process, as shown in Fig. 1. $(NH_4)_2V_3O_8$/C precursor was synthesized first through hydrothermal reaction [39], and the XRD pattern of the precursor is shown in Fig. S1, *Supplementary information*. Then the calcination process was taken in N_2 atmosphere to remove the ammonium and reduce the V (+4) to V (+3) using the organic carbon of the composites as the reductant. XRD patterns of the products calcined at different temperatures are shown in Fig. S2, *Supplementary information*. The reduction process was incomplete at a calcination temperature of 400 °C, resulting in the impurity of the product, such as VO_2 and V_8O_{15}, as well as low crystallinity. When the calcination temperature was over 500 °C, the product was well crystallized and all the diffraction peaks can be indexed to hexagonal V_2O_3 (JCPDS, No. 34-0187), denoting that the crystal product is pure V_2O_3, as shown in Fig. 2a. With increasing calcination temperature, the crystallinity of the product increased. When the calcination temperature rose to 800 °C, peaks belonging to VN (JCPDS, No. 65-5288) began to appear, which can be ascribed to the reaction between the vanadium species and N_2 at high temperature. No obvious peak of carbon species is observed in XRD patterns, indicating that carbon in the composites is amorphous. Product calcined at 700 °C, i.e. VO-C, was chosen for further characterization as it has the best crystallinity, which is beneficial for the ion diffusion between the layers. The average crystal size calculated from its XRD pattern based on the fitting of the whole spectrum using Scherrer equation is 25.8 nm, which can be a supporting evidence that the V_2O_3 particles in the composites are nano-sized.

FT-IR spectrum of VO-C is shown in Fig. 2b. Peaks at 3428 and 1627 cm^{-1} can be indexed to the stretching and bending vibration of O-H bonds of water. Peaks around 2885 and 2975 cm^{-1} are assigned to the stretching vibration of C-H bonds, of which peaks of bending vibration are located at around 1400 cm^{-1}. The peak at 1050 cm^{-1} corresponds to the asymmetrical stretching vibration of C-O. The peak at 987 cm^{-1} is the characteristic of V^{3+} caused by the symmetric stretching vibration of V^{3+}=O [35]. Peaks at 768 and 560 cm^{-1} are associated with the stretching vibration of V-O bonds. All these peaks indicate that the product consists of V_2O_3 and organic carbon. Raman spectrum was used to further investigate the composition of the composites. As labelled inset Fig. 2b, peaks with Raman shifts lower than 1000 cm^{-1} are all attributed to the

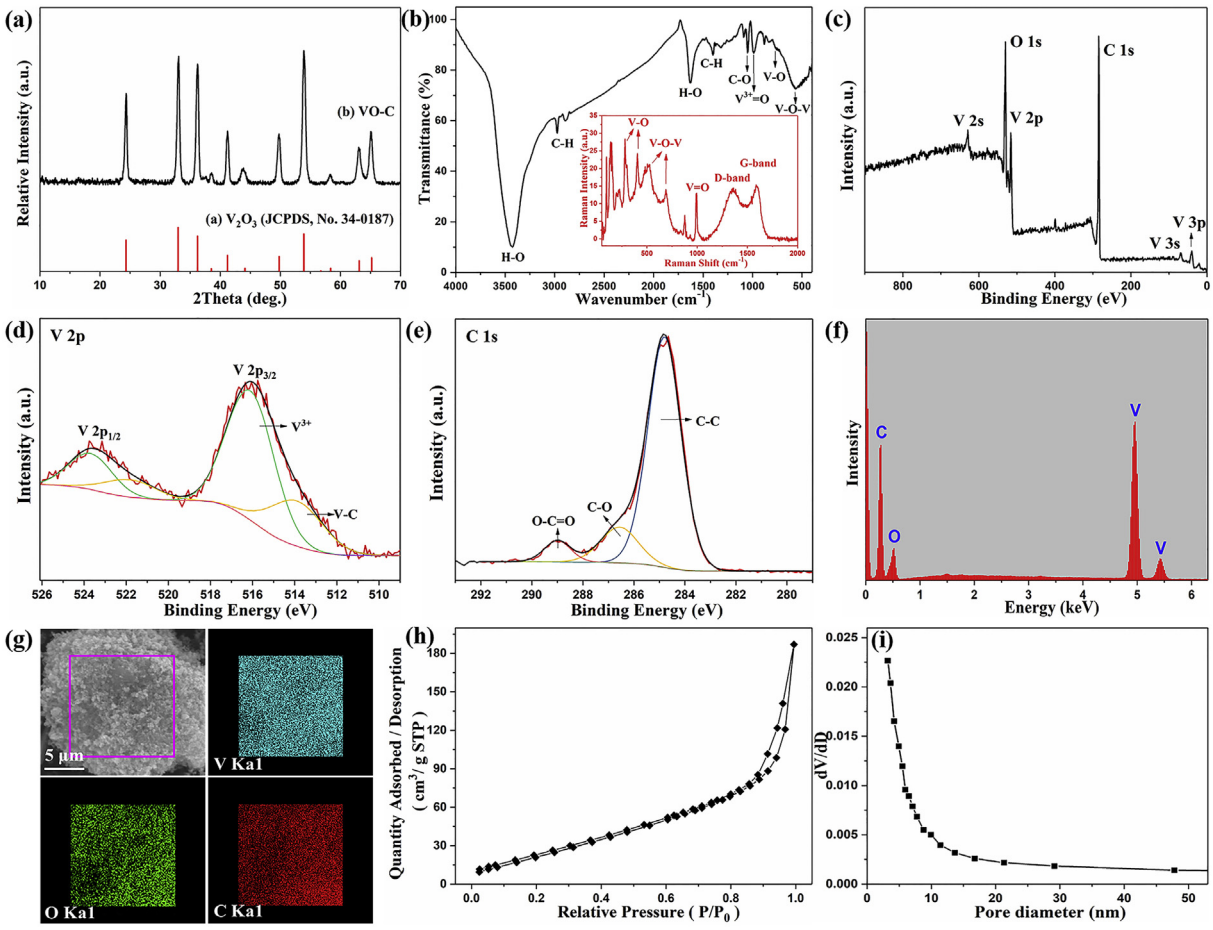

Fig. 2. (a) The XRD pattern of VO-C; (b) the FT-IR spectrum of VO-C, inset the Raman spectrum; (c-e) XPS spectra of VO-C: survey scan, V 2p and C1s; (f) EDS spectrum; (g) a SEM image and its corresponding elemental mapping images; (h, i): Nitrogen adsorption-desorption isotherms of VO-C and the corresponding pore size distribution data.

different modes of vibration of V_2O_3 [40]. Characteristic peaks of carbon, D-band and G band, are located at 1350 and 1585 cm^{-1} respectively. Both peaks are broad with a I_D/I_G value of 0.94, indicating the carbon is disordered with poor crystallinity, i.e. amorphous carbon. Both FT-IR and Raman spectra prove that carbon of the product is organic and amorphous.

Further information regarding the composition of VO-C was confirmed by XPS, EA, EDS and element mapping. V, O and C elements are clearly identified in full XPS spectrum (Fig. 2c). The two peaks in the V 2p core level spectrum (Fig. 2d) can be attributed to V $2p_{1/2}$ and V $2p_{3/2}$ respectively. The fitted peaks at 516.0 and 523.7 eV can be indexed to V $2p_{3/2}$ and V $2p_{1/2}$ of V^{3+} in V_2O_3 [41,42]. Peaks with lower binding energy (513.9 and 521.7 eV) can be attributed to V-C bond at the interface [43]. Besides, the bending energy of V^{2+} is also in this range [44,45]. As V^{2+} ions were formed when oxygen vacancies were generated near the surface [46,47]. These results indicate that the vanadium in the composites is mainly +3 state, while lower state can also be observed because of the surface modification, i.e. the combination of vanadium and carbon as well as the oxygen vacancies at the interface of vanadium oxide and carbon. C 1s spectrum (Fig. 2e) can be resolved into three peaks. Peaks at284.8, 286.6 and 290.0 eV are indexed to C-C of amorphous carbon, C-O species and O-C=O species, respectively [34,48]. EDS spectrum (Fig. 2f) also confirms that the composites are consist of C, O and V elements. The content of C is 46.4 wt%, which is much higher than the actual content (12.41 wt%) measured through EA, indicating that some carbon might coat on the V_2O_3. The mass fraction of V_2O_3 is further confirmed by TG-DSC curves, as shown in Fig. S3, *Supplementary information*. A small mass increase (1.8%) was observed between 120 and 270 °C, which is likely due to the partial oxidation of V_2O_3. From 270 to 540 °C, there was a rapid decrease of weight, attributable to the oxidation of carbon which is coated on vanadium oxide nanoparticles. At higher temperatures, the mass ratio increased to 94.6% and became stable after 620 °C, which is due to the formation of V_2O_5. The sharp endothermal DSC peak at 680 °C corresponds to the melt of V_2O_5. The mass fractions of V_2O_3 and organic carbon calculated based on the weight ratio of V_2O_5 are 78.0% and 22.0%, respectively. Elemental mapping images shown in Fig. 2g suggest the three elements are uniformly distributed in the sample. All above experimental data prove that the obtained product is a composite material consisting of surface modified V_2O_3 nanocrystals and amorphous carbon. To study the effect of ammonium on the product's pore structure, a comparative sample (V_2O_3-C) was synthesized in the same route as VO-C, but using V_2O_3 instead of NH_4VO_3 as raw material. The BET surface area of VO-C calculated from N_2 adsorption-desorption isotherms (Fig. 2h) is 106.8 $m^2\ g^{-1}$, which is higher than that of V_2O_3-C (66.5 $m^2\ g^{-1}$, Fig. S4a, *Supplementary information*). This result suggests that decomposition of NH_4VO_3 during the calcination is beneficial to the formation of new pores because of the release of the generated ammonia [36]. The pore size distribution calculated by the Barrett-Joyner-Halenda (BJH) method in Fig. 2i and Fig. S4b, *Supplementary information* shows that mesopores exist in both VO-C and V_2O_3-C. While VO-C

has higher percentage of pores with diameter less than 3.5 nm, indicating the releasing process of ammonia created small pores.

SEM images in Fig. 3a, b revealed that the product consists of nanoparticles with diameters of less than 50 nm, which are smaller compared that in the un-calcined precursor (about 80 nm, as shown in Fig. S5, *Supplementary information*). Furthermore, serious aggregation of the nanoparticles can be observed in the precursor because of the large amounts of carbon coating. While after calcination, each nanoparticle can be clearly observed. TEM images of the precursor (Fig. S6, *Supplementary information*) and VO-C (Fig. 3c–f) revealed the presence of mesopores. TEM images of VO-C also show that the diameter of V_2O_3 nanoparticles highly dispersed in the amorphous carbon is in the range of 7–30 nm, in a good agreement with the data calculated from XRD patterns (25.8 nm). Two different phases are also distinguished in HRTEM (Fig. 3f). The phase with obvious lattice is assigned to well crystallized V_2O_3, with inter-laminar spacing of 0.247 nm, corresponding to (1 1 0) plane. The amorphous carbon shows no lattice fringes, in consistent with no peak of carbon in XRD patterns. All these data indicated that VO-C are successfully synthesized, in which well crystallized V_2O_3 nanoparticles are highly dispersed in amorphous carbon.

3.2. Electrochemical properties of VO-C

The electrochemical performance of the synthesized VO-C as electrode material for supercapacitors was measured in a three-electrode experimental system. CV curves collected at different scan rates are shown in Fig. 4a. Two pairs of redox peaks can be observed when the scan rate is 5 mV s^{-1}, as shown in Fig. S7, *Supplementary information*. While as the scan rate increases, the redox peaks shift slightly, indicating the increasing degree of electrode polarization. The redox peaks still exist when the scan rate increases to 100 mV s^{-1}, suggesting a good ionic and electronic conduction [1]. The charging mechanism of VO-C can be further analyzed by the following equation [49,50]:

$$i = av^b \tag{7}$$

in which i is the peak current, v is the scan rate, a and b are both adjustable parameters. If $b = 0.5$, the electrochemical process is totally controlled by the bulk diffusion process, which means that the electrode material is typical battery-type. Whereas b = 1 indicates a surface reaction-controlled capacitive behavior. The b value can be calculated by evaluating the logarithm and linear fitting of i and v, as shown in Fig. 4b. In this case, the slope of $\log(i) - \log(v)$ plot of the VO-C electrode peaks (marked with arrow in Fig. 4a) is 0.931, which is close to 1, demonstrating a hybrid charge storage mechanism. As amorphous carbon shows negligible double-layer capacitance (Fig. 4d), most of the capacitance arises from the pseudocapacitance of V_2O_3 [11,35]. To further investigate the charge storage mechanism of V_2O_3, *ex-suit* XRD patterns of the initial electrode and electrodes after 2 cycles of CV at a scan rate of 5 mV/s were taken, as shown in Fig. S8, *Supplementary information*. No significant change was observed, suggesting there is neither the formation of new phase nor disappearance of existing phase during the charge-discharge process. While compared with the initial and charged to −0.3 V electrodes, the peaks of the electrode discharged to −1 V have a slight shift to the left at high angles (insert Fig. S8), which indicates a subtle expansion of lattice constants, and suggests the redox reactions are likely due to the intercalation reaction. The intercalation pseudocapacitance is imply referred to the capacitance arising from intercalation redox reaction in the bulk material, while its kinetics is limited by surface reaction process instead of the diffusion of ions in the bulk material. The shift of peaks is not obvious in this work because Li^+ is much smaller than K^+, leading to a less expansion of lattice [42,51]. Besides, the Coulomb attraction force between inserted Li cations and O anions in the host crystal would counter act the expansion of the lattice space. The inferred electrochemical redox reaction is as follow:

$$V_2O_3 + xLi^+ + xe^- \rightleftharpoons Li_xV_2O_3 \tag{8}$$

Though the intercalation pseudocapacitance is generated by the battery-type intercalation/de-intercalation of electrolyte ions in the interlayer of crystalline V_2O_3, which can be proved by the redox peaks in the CV curves, the kinetics of this process is predominantly surface reaction controlled and similar to the pseudocapacitive behavior [11]. For comparison, CV curves of VO+C at different scan rates are also measured, as shown in Fig. S9, *Supplementary information*. The peaks displacement is more pronounced as compared with that of VO-C. Moreover, the b value of the same redox peaks in VO+C is 0.635 (Fig. 4b), indicating a slow diffusion rate. The excellent diffusion rate in VO-C is attributed to the special structure of the composites. First, the open, layered structure of crystalline V_2O_3 enables fast ion diffusion on the 2-D plane. Second, the highly dispersed V_2O_3 nanoparticles provide large interface between the active material and the electrolyte, which can shorten the pathway

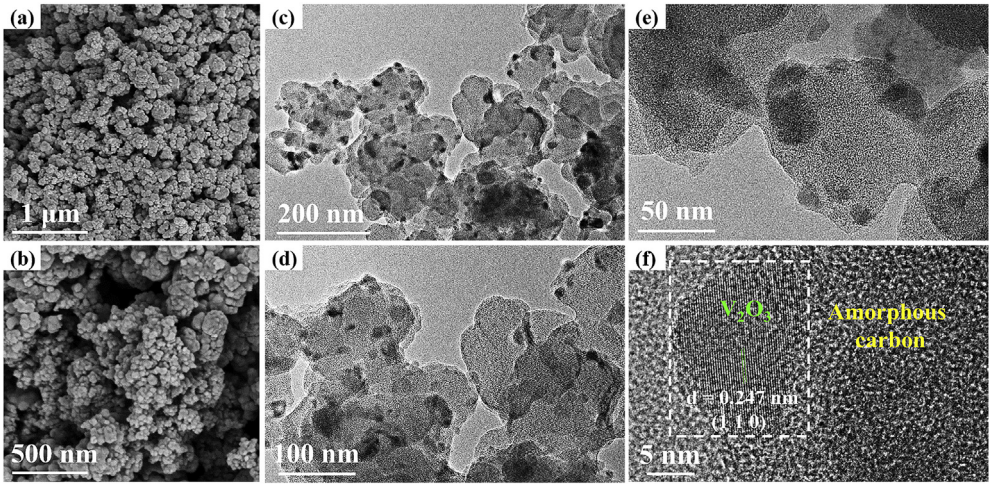

Fig. 3. SEM images (a, b) and TEM images (c-f) of the synthesized VO-C.

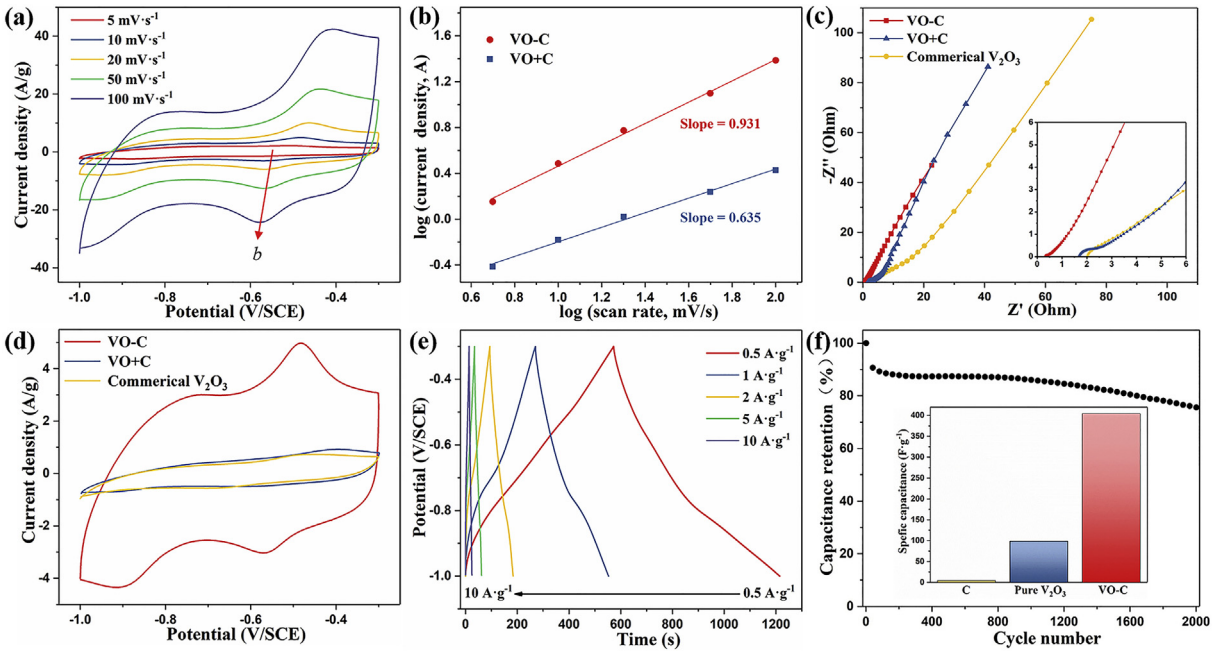

Fig. 4. (a) CV curves of the VO-C electrode collected at different scan rates; (b) determination of the b-value of peak currents of VO-C and VO+C; (c-d): comparison of VO-C, VO+C and commercial V_2O_3: CV curves collected at 10 mV s^{-1} (c) and Nyquist plots in the frequency range from 100 kHz to 0.01 Hz (d); (e) GCD curves of VO-C collected at different current densities; inset the comparison of the capacitances of amorphous carbon, pure V_2O_3 and VO-C; (f) Cycling performance of the VO-C electrode measured at 100 mV s^{-1} for 2000 cycles, inset the comparison of the capacitances of amorphous carbon, pure V_2O_3 and VO-C.

of ion diffusion. Third, highly porous carbon matrix provided minimized electric polarization. All these factors led the extremely fast ion diffusion rate in the electrode material, so the kinetics of the energy storage process is predominantly pseudocapacitive.

The EIS of VO-C is shown in Fig. 4c. The high slope of the Nyquist plot of VO-C at low frequencies indicates fast diffusion of ions in the active material [27]. The calculated ion diffusion coefficients of VO-C, VO+C and commercial V_2O_3 using equation (1) are $1.02*10^{-11}$, $3.65*10^{-12}$ and $1.26*10^{-12}$ cm^2 s^{-1}, respectively. The fitting of Z'-$\omega^{-1/2}$ is shown in Fig. S10, *Supplementary information*. This result indicates that physically mixed with amorphous carbon can only improve the ion transfer rate slightly, even though the synthesized carbon has a large surface area of 367.4 m^2 g^{-1} (Fig. S11, *Supplementary information*). In high frequencies, the intersection of the plot at *x*-axis represents the equivalent series resistance (R_s). The R_s of VO-C is about 0.34 Ω, which is lower than that of VO+C (1.68 Ω) and commercial (2.02 Ω), revealing the lowest intrinsic resistance of the composites [52]. The semicircle that represents the charge transfer resistance (R_{ct}) is negligible in VO-C; while an obvious semicircle occurred in VO+C, demonstrating the surface modification played a pivotal role in the acceleration of electron transfer in the composites. Oxygen vacancies could facilitate the electron transfer by narrowed the band gap of the metal oxides [53,54]; the low valence vanadium ions (divalent) induced simultaneously when oxygen vacancies are formed to maintain the electroneutrality are likely to introduce the hoping conduction. Besides, the V-C bond at the interface allows the unobstructed pass of electron between these two compositions. While though VO+C consists of the same composition, the physical mixing of VO and C would not improve the conductivity, but created barriers among V_2O_3 particles, leading to a larger R_{ct} than that in pure V_2O_3. Low resistance, excellent ion and electron transfer efficiency would lead to a significantly enhanced specific capacitance, as shown in Fig. 4d and inset of Fig. 4f.

The GCD curves of VO-C collected at various current densities are shown in Fig. 4e. The specific capacitance of the electrode calculated according to equation (2) is 458.6 F g^{-1} at a current density of 0.5 A g^{-1}, which is much higher than the reported V_2O_3 and carbon composites (as shown in Table 1), and comparable with that of MoS_2 coated V_2O_3 composite (485 F g^{-1} at 0.5 A g^{-1}) [55]. A synergistic effect exists between vanadium oxides and moderate amount of carbon, which can significantly improve the specific

Table 1
Comparison of the electrochemical performance of V_2O_3/C composites with important literature reports.

Types of V_2O_3 material	Electrolyte	Specific capacitance /F·g^{-1}	Cyclic performance	References
VO-C nanocomposites	5 M LiCl	458, 0.5 A g^{-1}	86% after 1000 cycles	This work
V_2O_3@C core-shell nanorods	5 M LiCl	228, 0.5 A g^{-1}	81% after 1000 cycles	[36]
V_2O_3 nanoflakes @C composites	1 M $NaNO_3$	205, 0.05 A g^{-1}	76% after 500 cycles	[35]
V_2O_3/N-rGO composites	1 M Na_2SO_4	206, 1 mA cm^{-2}	-	[56]
V_2O_3@C core-shell composites	1 M Na_2SO_4	180, 0.5 A g^{-1}	39.7% after 100 cycles	[57]
V_2O_3@C core-shell nanorods	1 M Na_2SO_4	192, 1 A g^{-1}	66% after 1000 cycles	[58]
V_2O_3 nanofoam @ C composites	1 M $NaNO_3$	185, 0.05 A g^{-1}	49% after 100 cycles	[59]
V_2O_3-MWCNT composites	0.5 M Na_2SO_4	147, 2 mV s^{-1}	78% after 1000 cycles	[60]
V_2O_3/VO_2/C composites	1 M KNO_3	171, 0.1 A g^{-1}	-	[61]
MoS_2 coated V_2O_3 composite	1 M Na_2SO_4	485, 0.5 A g^{-1}	-	[55]

capacitance of the composites as suggested in literature [31,51]. Though the amorphous carbon exhibits a quite low capacitance (5 F g^{-1} at 1 A g^{-1}, as shown inset Fig. 4f), it can provide efficient pathways for the conductivity of the active material [34,36] and result in a much higher specific capacitance than pure V_2O_3 (99 F g^{-1} at 1 A g^{-1}). When the current densities are 1, 2, 5 and 10 A g^{-1}, the corresponding specific capacitances are 404.7, 254.6, 188.6 and 147.1 F g^{-1}, respectively. Incremental IR drop is observed at high current densities, confirming the good conductivity of the electrode, which is consistent with the EIS results.

Cycling stability of the electrode was measured at a scan rate of 100 mV s^{-1}. The capacitance suffers a rapid decline to 90.7% of the initial capacitance after 40 cycles (Fig. 4f) which might be ascribed to some irreversible electrochemical process. Then the capacitance represents a slightly fluctuating decline to 86% of the initial capacitance after 1000 cycles and 75.6% after 2000 cycles, which is a satisfactory performance compared with other vanadium oxides-based materials, especially those in aqueous electrolytes [62–64]. Vanadium oxides species usually suffer poor cycling stabilities because of their unavoidable dissolution in aqueous solutions [65]. The initial release rate of V_2O_3 is about $3.5^{*}10^{-2}$ mmol m^{-2} h^{-1} when the PH is 7 (5 M LiCl) [66]. The carbon coating could enhance the stability of V_2O_3 nanoparticles by avoiding the structure degradation and limited the direct contact between V_2O_3 and aqueous electrolyte without affecting the ion transfer. However, the slow dissolution of V_2O_3 can still proceed and lead to slow capacitance decay [67]. The degradation of layered structures during the ions intercalation/de-intercalation in the cycling process is another reason for the irreversible capacity loss of vanadium oxides [68].

3.3. Electrochemical performance of ASC devices

Flexible asymmetric supercapacitors (ASCs) were assembled by combining the electrodes of VO-C and active carbon, as shown inset Fig. 5c. CV curves of the ASC device measured at different scan rates in the potential range of 0–0.7 V (shown in Fig. 5a) exhibit quasi-rectangular shapes without severe distortion even at a high scan rate of 100 mV s^{-1}, suggesting the excellent capacitive behavior of the device [69]. The areal capacitances calculated from the CV curves collected at 5, 10, 20, 50, 100 mV s^{-1} are 262, 220, 183, 141 and 113 mF cm^{-2}, respectively. The Ragone plot of the device (Fig. 5b) shows that the ASC device exhibits a maximum energy density of 0.145 W h m^{-2} and a corresponding power density of 1.43 W m^{-2} at a current density of 0.5 mA cm^{-2}. The Nyquist plot of the device is shown in Fig. S12, *Supplementary information*. At low frequencies, the high slope confirms the excellent rate of ion diffusion in the bulk of electrode material, which is consistent with the result of a three-electrode system [70]. As the R_s of the system is determined not only by the intrinsic resistance of active materials, but also by the resistance of the electrolyte, the higher R_s (2.7 Ω) of the device compared with the result in three-electrode could be attributed to the increasing electrolyte resistance because of the addition of PVA [71]. However, the small increase of R_{ct} suggests the addition of PVA did not have much influence on the interface conductivity of the electrolyte and the electrode materials.

The mechanical flexibility of the device is proven by testing the CV curves of the device at different bend conditions, as shown in Fig. 5c. The capacitances are almost constant while bending the device, demonstrating the device is flexible. A red light emitting diode (LED) was lit by a series of four devices in order to reach the standard voltage of the LED, as shown inset Fig. 5d and in Fig. S13,

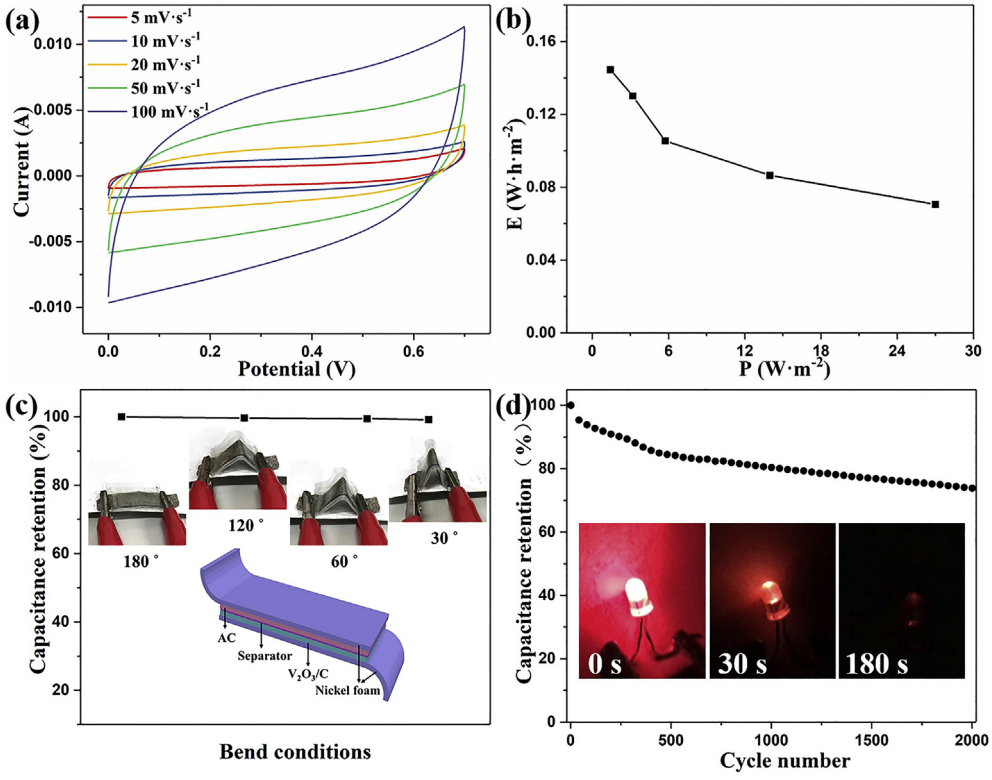

Fig. 5. Electrochemical performance of the ASC device assembled by VO-C//AC: (a) CV curves collected at different scan rates; (b) the Ragone plot; (c) capacitance retention of the VO-C//AC device measured under different bend conditions, inset is a schematic illustrating the configuration of the ASC device; (d) cycling performance measured at 100 mV s^{-1} for 2000 cycles, inset are pictures of the ASC devices lighting a red LED. (For interpretation of the references to colour in this figure legend, the reader is referred to the Web version of this article.)

Supplementary information. The LED illuminated for more than 180 s, indicating the assembled ASCs function well in practical applications. Cycling performance of the devices is measured by CV at a scan rate of 100 mV s^{-1}, and the calculated result is shown in Fig. 5d. Similar to the phenomenon observed in the three-electrode system, the device also suffers a rapid decline of over 15% at the first 500 cycles. Then a slow reduction can be observed in the next 1500 cycles with a whole retention of 73.9% after 2000 cycle. All the above analyses reveal that VO-C can be a promising electrode material for supercapacitors in practical application.

4. Conclusions

V_2O_3 nanoparticles highly dispersed in amorphous carbon composites were designed and synthesized through the calcination of fabricated $(NH_4)_2V_3O_8$/C composites using NH_4VO_3 and glucose as the vanadium and carbon sources, respectively. The resulting VO-C composites composed of nanocrystal V_2O_3 with surface defects highly dispersed in porous amorphous carbon. The energy storage mechanism was studied. The composites exhibited a high intercalation pseudocapacitance of 458.6 F g^{-1} at 0.5 A g^{-1} due to the unique highly dispersed microstructure, and the high ion diffusion and charge transfer rate attributed to the promoted surface properties of V_2O_3. The composites exhibited an excellent cycling stability with a retention of 86% after 1000 cycles in aqueous electrolyte. The flexible ASC device assembled by VO-C and active carbon was characterized. This work suggests that V_2O_3 can be a promising electrode material for supercapacitors with excellent electrochemical properties. Meanwhile, creating surface defects at the interface of the composite can significantly enhance its electrochemical properties by improving the conductivity of the composites. The work also proves that employing a highly dispersed architecture is an effective way to realize the high utilization of metal oxides, thus improving the specific capacitance and stability of the active material.

Conflicts of interest

There are no conflicts of interest to declare.

Acknowledgements

This work was partially supported by the National Natural Science Foundation of China, China, (Grant No. 21601026, 21771030), Fundamental Research Funds for the Central Universities, China, (DUT16RC(4)10, DUT18RC(6)008), and Doctoral Research Foundation of Liaoning Province, China, (No. 201601035). This work was also supported in part by the National Science Foundation, Unitated States, (No. 1803256). J. Zheng acknowledges the financial support from China Scholarship Council, China, (No. 201806060032).

Appendix A. Supplementary data

Supplementary data to this article can be found online at https://doi.org/10.1016/j.electacta.2019.06.125.

References

[1] X. Lu, M. Yu, G. Wang, Y. Tong, Y. Li, Flexible solid-state supercapacitors: Design, fabrication and applications, Energy Environ. Sci. 7 (2014) 2160–2181.
[2] A. Gonzalez, E. Goikolea, J.A. Barrena, R. Mysyk, Review on supercapacitors: Technologies and materials, Renew. Sustain. Energy Rev. 58 (2016) 1189–1206.
[3] P. Simon, Y. Gogotsi, Materials for electrochemical capacitors, Nat. Mater. 7 (2008) 845–854.
[4] W. Liu, M.S. Song, B. Kong, Y. Cui, Flexible and stretchable energy storage: Recent advances and future perspectives, Adv. Mater. 29 (2017) 34.
[5] Y. Han, Z. Lai, Z. Wang, M. Yu, Y. Tong, X. Lu, Designing carbon based supercapacitors with high energy density: A summary of recent progress, Chem. Eur J. 24 (2018) 7312–7329.
[6] Y. Zhang, H. Jiang, Q. Wang, C. Meng, In-situ hydrothermal growth of $Zn_4Si_2O_7(OH)_2 \cdot H_2O$ anchored on 3D N, S-enriched carbon derived from plant biomass for flexible solid-state asymmetrical supercapacitors, Chem. Eng. J. 352 (2018) 519–529.
[7] G. Wang, L. Zhang, J. Zhang, A review of electrode materials for electrochemical supercapacitors, Chem. Soc. Rev. 41 (2012) 797–828.
[8] M. Yu, Z. Wang, Y. Han, Y. Tong, X. Lu, S. Yang, Recent progress in the development of anodes for asymmetric supercapacitors, J. Mater. Chem. 4 (2016) 4634–4658.
[9] Q. Wang, Y. Zhang, H. Jiang, X. Li, Y. Cheng, C. Meng, Designed mesoporous hollow sphere architecture metal (Mn, Co, Ni) silicate: A potential electrode material for flexible all solid-state asymmetric supercapacitor, Chem. Eng. J. 362 (2019) 818–829.
[10] T. Brousse, D. Belanger, J.W. Long, To be or not to be pseudocapacitive? J. Electrochem. Soc. 162 (2015) A5185–A5189.
[11] Y. Wang, Y. Song, Y. Xia, Electrochemical capacitors: Mechanism, materials, systems, characterization and applications, Chem. Soc. Rev. 45 (2016) 5925–5950.
[12] M. Salanne, B. Rotenberg, K. Naoi, K. Kaneko, P.L. Taberna, C.P. Grey, B. Dunn, P. Simon, Efficient storage mechanisms for building better supercapacitors, Nat. Energy 1 (2016) 10.
[13] T. Brezesinski, J. Wang, S.H. Tolbert, B. Dunn, Ordered mesoporous α-MoO_3 with iso-oriented nanocrystalline walls for thin-film pseudocapacitors, Nat. Mater. 9 (2010) 146.
[14] F. Wang, X. Wu, X. Yuan, Z. Liu, Y. Zhang, L. Fu, Y. Zhu, Q. Zhou, Y. Wu, W. Huang, Latest advances in supercapacitors: From new electrode materials to novel device designs, Chem. Soc. Rev. 46 (2017) 6816–6854.
[15] Y. Zhang, M. Chen, T. Hu, C. Meng, 3D interlaced networks of $VO(OH)_2$ nanoflakes wrapped with graphene oxide nanosheets as electrodes for energy storage devices, ACS Appl. Nano Mater. 2 (2019) 2934–2945.
[16] M. Zukalová, M. Kalbáč, L. Kavan, I. Exnar, M. Graetzel, Pseudocapacitive lithium storage in TiO_2(B), Chem. Mater. 17 (2005) 1248–1255.
[17] Y. Wang, Z. Hong, M. Wei, Y. Xia, Layered $H_2Ti_6O_{13}$-nanowires: A new promising pseudocapacitive material in non-aqueous electrolyte, Adv. Funct. Mater. 22 (2012) 5185–5193.
[18] H. Hosseini, S. Shahrokhian, Vanadium dioxide-anchored porous carbon nanofibers as a Na^+ intercalation pseudocapacitance material for development of flexible and super light electrochemical energy storage systems, Appl. Mater. Today 10 (2018) 72–85.
[19] N.A. Chernova, M. Roppolo, A.C. Dillon, M.S. Whittingham, Layered vanadium and molybdenum oxides: Batteries and electrochromics, J. Mater. Chem. 19 (2009) 2526–2552.
[20] Y. Yan, B. Li, W. Guo, H. Pang, H. Xue, Vanadium based materials as electrode materials for high performance supercapacitors, J. Power Sources 329 (2016) 148–169.
[21] P. Liu, K. Zhu, Y. Gao, H. Luo, L. Lu, Recent progress in the applications of vanadium-based oxides on energy storage: From low-dimensional nanomaterials synthesis to 3D micro/nano-structures and free-standing electrodes fabrication, Adv. Energy Mater. 7 (2017) 1700547.
[22] X. Pan, G. Ren, M.N.F. Hoque, S. Bayne, K. Zhu, Z. Fan, Fast supercapacitors based on graphene-bridged V_2O_3/VOx core-shell nanostructure electrodes with a power density of 1 MW kg(-1), Adv. Mater. Interf. 1 (2014).
[23] K. Dahal, Q. Zhang, R. He, I.K. Mishra, Z. Ren, Thermal conductivity of $(VO_2)_{1-x}Cu_x$ composites across the phase transition temperature, J. Appl. Phys. 121 (2017) 155103.
[24] X. Liu, Y. Hu, G. Jia, H. Zhang, H. Jiang, C. Li, Homologous V_2O_3/C box-in-box and V_2O_5 box for lithium-ion full cells, J. Mater. Chem. 4 (2016) 12030–12035.
[25] J. Wang, Z. Liu, W. Yang, L. Han, M. Wei, A one-step synthesis of porous V_2O_3@C hollow spheres as a high-performance anode for lithium-ion batteries, Chem. Commun. 54 (2018) 7346–7349.
[26] Y. Wang, H.J. Zhang, A.S. Admar, J. Luo, C.C. Wong, A. Borgna, J. Lin, Improved cyclability of lithium-ion battery anode using encapsulated V_2O_3 nanostructures in well-graphitized carbon fiber, RSC Adv. 2 (2012) 5748–5753.
[27] M. Yu, Y. Zeng, Y. Han, X. Cheng, W. Zhao, C. Liang, Y. Tong, H. Tang, X. Lu, Valence-optimized vanadium oxide supercapacitor electrodes exhibit ultrahigh capacitance and super-long cyclic durability of 100 000 cycles, Adv. Funct. Mater. 25 (2015) 3534–3540.
[28] G.M. Wang, X.H. Lu, Y.C. Ling, T. Zhai, H.Y. Wang, Y.X. Tong, Y. Li, LiCl/PVA gel electrolyte stabilizes vanadium oxide nanowire electrodes for pseudocapacitors, ACS Nano 6 (2012) 10296–10302.
[29] X. Li, J. Fu, Z. Pan, J. Su, J. Xu, B. Gao, X. Peng, L. Wang, X. Zhang, P.K. Chu, Peapod-like V_2O_3 nanorods encapsulated into carbon as binder-free and flexible electrodes in lithium-ion batteries, J. Power Sources 331 (2016) 58–66.
[30] D. Majumdar, M. Mandal, S.K. Bhattacharya, V_2O_5 and its carbon-based nanocomposites for supercapacitor applications, ChemElectroChem 6 (2019) 1623–1648.
[31] B. Saravanakumar, K.K. Purushothaman, G. Muralidharan, High performance supercapacitor based on carbon coated V_2O_5 nanorods, J. Electroanal. Chem. 758 (2015) 111–116.
[32] D. Zhao, Q. Zhu, D. Chen, X. Li, Y. Yu, X. Huang, Nest-like V_3O_7 self-assembled by porous nanowires as an anode supercapacitor material and its

performance optimization through bonding with N-doped carbon, J. Mater. Chem. 6 (2018) 16475–16484.
[33] Y. Zhang, J. Zheng, T. Hu, F. Tian, C. Meng, Synthesis and supercapacitor electrode of VO_2(B)/C core-shell composites with a pseudocapacitance in aqueous solution, Appl. Surf. Sci. 371 (2016) 189–195.
[34] J. Zheng, Y. Zhang, Q. Wang, H. Jiang, Y. Liu, T. Lv, C. Meng, Hydrothermal encapsulation of VO_2(A) nanorods in amorphous carbon by carbonization of glucose for energy storage devices, Dalton Trans. 47 (2018) 452–464.
[35] H.-Y. Li, K. Jiao, L. Wang, C. Wei, X. Li, B. Xie, Micelle anchored in situ synthesis of V_2O_3 nanoflakes@C composites for supercapacitors, J. Mater. Chem. A 2 (2014) 18806–18815.
[36] T. Hu, Y. Liu, Y. Zhang, Y. Nie, J. Zheng, Q. Wang, H. Jiang, C. Meng, Encapsulating V_2O_3 nanorods into carbon core-shell composites with porous structures and large specific surface area for high performance solid-state supercapacitors, Microporous Mesoporous Mater. 262 (2018) 199–206.
[37] C. Liu, H. Fu, Y. Pei, J. Wu, V. Pisharodi, Y. Hu, G. Gao, R.J. Yang, J. Yang, G. Cao, Understanding the electrochemical potential and diffusivity of MnO/C nanocomposites at various charge/discharge states, J. Mater. Chem. 7 (2019) 7831–7842.
[38] C. Liu, S. Wang, C. Zhang, H. Fu, X. Nan, Y. Yang, G. Cao, High power high safety battery with electrospun $Li_3V_2(PO_4)_3$ cathode and $Li_4Ti_5O_{12}$ anode with 95% energy efficiency, Energy Storage Mater. 5 (2016) 93–102.
[39] Y. Zhang, J. Zheng, Q. Wang, S. Zhang, T. Hu, C. Meng, One-step hydrothermal preparation of $(NH_4)_2V_3O_8$/carbon composites and conversion to porous V_2O_5 nanoparticles as supercapacitor electrode with excellent pseudocapacitive capability, Appl. Surf. Sci. 423 (2017) 728–742.
[40] W. Zhu, R. Li, P. Xu, Y. Li, J. Liu, Vanadium trioxide@carbon nanosheet array-based ultrathin flexible symmetric hydrogel supercapacitors with 2 V voltage and high volumetric energy density, J. Mater. Chem. 5 (2017) 22216–22223.
[41] B. Long, M.-S. Balogun, L. Luo, Y. Luo, W. Qiu, S. Song, L. Zhang, Y. Tong, Encapsulated vanadium-based hybrids in amorphous N-doped carbon matrix as anode materials for lithium-ion batteries, Small 13 (2017) 1702081.
[42] T. Jin, H. Li, Y. Li, L. Jiao, J. Chen, Intercalation pseudocapacitance in flexible and self-standing V_2O_3 porous nanofibers for high-rate and ultra-stable K ion storage, Nanomater. Energy 50 (2018) 462–467.
[43] T. Huang, J. Yu, J. Han, Z. Zhang, Y. Xing, C. Wen, X. Wu, Y. Zhang, Oxygen reduction catalytic characteristics of vanadium carbide and nitrogen doped vanadium carbide, J. Power Sources 300 (2015) 483–490.
[44] E. Hryha, E. Rutqvist, L. Nyborg, Stoichiometric vanadium oxides studied by XPS, Surf. Interface Anal. 44 (2012) 1022–1025.
[45] G. Silversmit, D. Depla, H. Poelman, G.B. Marin, R. De Gryse, Determination of the V2p XPS binding energies for different vanadium oxidation states (V5+ to V0+), J. Electron. Spectrosc. Relat. Phenom. 135 (2004) 167–175.
[46] H. Song, C. Liu, C. Zhang, G. Cao, Self-doped V^{4+}–V_2O_5 nanoflake for 2 Li-ion intercalation with enhanced rate and cycling performance, Nanomater. Energy 22 (2016) 1–10.
[47] W. Ma, C. Zhang, C. Liu, X. Nan, H. Fu, G. Cao, Impacts of surface energy on lithium ion intercalation properties of V_2O_5, ACS Appl. Mater. Interfaces 8 (2016) 19542–19549.
[48] L. Jiang, Y. Qu, Z. Ren, P. Yu, D. Zhao, W. Zhou, L. Wang, H. Fu, In situ carbon-coated yolk–shell V_2O_3 microspheres for lithium-ion batteries, ACS Appl. Mater. Interfaces 7 (2015) 1595–1601.
[49] J. Wang, J. Polleux, J. Lim, B. Dunn, Pseudocapacitive contributions to electrochemical energy storage in TiO_2 (anatase) nanoparticles, J. Phys. Chem. C 111 (2007) 14925–14931.
[50] L. Kong, C. Zhang, J. Wang, W. Qiao, L. Ling, D. Long, Free-Standing T-Nb_2O_5/graphene composite papers with ultrahigh gravimetric/volumetric capacitance for Li-ion intercalation pseudocapacitor, ACS Nano 9 (2015) 11200–11208.
[51] S. Tan, Y. Jiang, Q. Wei, Q. Huang, Y. Dai, F. Xiong, Q. Li, Q. An, X. Xu, Z. Zhu, X. Bai, L. Mai, Multidimensional synergistic nanoarchitecture exhibiting highly stable and ultrafast sodium-ion storage, Adv. Mater. 30 (2018) 1707122.
[52] J.L. Qi, X. Wang, J.H. Lin, F. Zhang, J.C. Feng, W.D. Fei, Vertically oriented few-layer graphene-nanocup hybrid structured electrodes for high-performance supercapacitors, J. Mater. Chem. 3 (2015) 12396–12403.
[53] W. Bi, Y. Wu, C. Liu, J. Wang, Y. Du, G. Gao, G. Wu, G. Cao, Gradient oxygen vacancies in V_2O_5/PEDOT nanocables for high-performance supercapacitors, ACS Appl. Energy Mater. 2 (2019) 668–677.
[54] Y. Wang, J. Li, Z. Wei, Transition-metal-oxide-based catalysts for the oxygen reduction reaction, J. Mater. Chem. 6 (2018) 8194–8209.
[55] H. Peng, T. Liu, Y. Li, X. Wei, X. Cui, Y. Zhang, P. Xiao, Hierarchical MoS_2-Coated V_2O_3 composite nanosheet tubes as both the cathode and anode materials for pseudocapacitors, Electrochim. Acta 277 (2018) 218–225.
[56] Z.Q. Hou, Z.Y. Wang, L.X. Yang, Z.G. Yang, Nitrogen-doped reduced graphene oxide intertwined with V_2O_3 nanoflakes as self-supported electrodes for flexible all-solid-state supercapacitors, RSC Adv. 7 (2017) 25732–25739.
[57] J. Zheng, Y. Zhang, X. Jing, X. Liu, T. Hu, T. Lv, S. Zhang, C. Meng, Synthesis of amorphous carbon coated on V_2O_3 core-shell composites for enhancing the electrochemical properties of V_2O_3 as supercapacitor electrode, Colloid. Surf. Physicochem. Eng. Asp. 518 (2017) 188–196.
[58] Y. Zhang, Designed synthesis and supercapacitor electrode of V_2O_3@C core-shell structured nanorods with excellent pseudo-capacitance in Na_2SO_4 neutral electrolyte, Chemistryselect 3 (2018) 1577–1584.
[59] X. Zhang, Z. Bu, R. Xu, B. Xie, H.-Y. Li, V_2O_3 nanofoam@activated carbon composites as electrode materials of supercapacitors, Funct. Mater. Lett. 10 (2017).
[60] C.J. Wallar, R. Poon, I. Zhitomirsky, High areal capacitance of V_2O_3-carbon nanotube electrodes, J. Electrochem. Soc. 164 (2017) A3620–A3627.
[61] C. Zhao, J. Cao, Y. Yang, W. Chen, J. Li, Facile synthesis of hierarchical porous VOx@carbon composites for supercapacitors, J. Colloid Interface Sci. 427 (2014) 73–79.
[62] Y. Zhang, J. Zheng, T. Hu, F. Tian, C. Meng, Synthesis and supercapacitor electrode of VO_2(B)/C core–shell composites with a pseudocapacitance in aqueous solution, Appl. Surf. Sci. 371 (2016) 189–195.
[63] Y. Zhang, J. Zheng, Y. Zhao, T. Hu, Z. Gao, C. Meng, Fabrication of V_2O_5 with various morphologies for high-performance electrochemical capacitor, Appl. Surf. Sci. 377 (2016) 385–393.
[64] Y. Zhang, X. Jing, Q. Wang, J. Zheng, H. Jiang, C. Meng, Three-dimensional porous V_2O_5 hierarchical spheres as a battery-type electrode for a hybrid supercapacitor with excellent charge storage performance, Dalton Trans. 46 (2017) 15048–15058.
[65] J. Zheng, Y. Zhang, T. Hu, T. Lv, C. Meng, New strategy for the morphology-controlled synthesis of V_2O_5 microcrystals with enhanced capacitance as battery-type supercapacitor electrodes, Cryst. Growth Des. 18 (2018) 5365–5376.
[66] X. Hu, Y. Yue, X. Peng, Release kinetics of vanadium from vanadium (III, IV and V) oxides: Effect of pH, temperature and oxide dose, J. Environ. Sci. 67 (2018) 96–103.
[67] X. Lu, T. Liu, T. Zhai, G. Wang, M. Yu, S. Xie, Y. Ling, C. Liang, Y. Tong, Y. Li, Improving the cycling stability of metal-nitride supercapacitor electrodes with a thin carbon shell, Adv. Energy Mater. 4 (2014) 1300994.
[68] X.Y. Zhang, M.H. Yu, S.B. Zhao, F. Li, X.L. Hu, S.B. Guo, X.H. Lu, Y.X. Tong, 3D V_3O_7 center dot H_2O/partially exfoliated carbon nanotube composites with significantly improved lithium storage ability, Part. Part. Syst. Char. 33 (2016) 7.
[69] Y. Zhang, J. Zheng, X. Jing, C. Meng, A strategy for the synthesis of VN@C and VC@C core-shell composites with hierarchically porous structures and large specific surface areas for high performance symmetric supercapacitors, Dalton Trans. 47 (2018) 8052–8062.
[70] Y. Zhang, H. Jiang, Q. Wang, J. Zheng, C. Meng, Kelp-derived three-dimensional hierarchical porous N, O-doped carbon for flexible solid-state symmetrical supercapacitors with excellent performance, Appl. Surf. Sci. 447 (2018) 876–885.
[71] J.L. Qi, X. Wang, J.H. Lin, F. Zhang, J.C. Feng, W.-D. Fei, A high-performance supercapacitor of vertically-oriented few-layered graphene with high-density defects, Nanoscale 7 (2015) 3675–3682.